J-integral for Natural Rubber compounds via Digital Image Correlation

Francesco Caimmi[a,*], Roberto Calabrò[a], Claudia Marano[a], Marta Rink[a]

[a]*Chemistry, Materials and Chemical Engineering Department "Giulio Natta", Politecnico di Milano, P.za Leonardo da Vinci 32, I-20133 Milano, Italy*

[*] Corresponding author: Tel. +39 02 2399 4711 Fax +39 02 7063 8173 Email address: francesco.caimmi@polimi.it (Francesco Caimmi)

Abstract

The application of the Digital Image Correlation technique to the determination of the *J*-integral at fracture initiation for carbon-black filled natural rubber compounds is discussed. Three different compounds with varying carbon black content were tested, using two different tests: pure shear and biaxial tensile test. Digital image correlation was used to measure the displacement field around the crack tip in the tested specimens. From the displacement field, which is interpolated using a finite element scheme, the stresses were evaluated by using Ogden's hyperelastic model, and the *J*-integral could be calculated. The results compare well with both theoretical and finite element results.

Keywords: Natural Rubber Compounds, *J*-integral, Fracture, Digital Image Correlation

1. Introduction

The application of digital image correlation (DIC) techniques [1] to the measurement of mechanical parameters dates back to the early ’80s [2–4] and it’s getting more and more widespread (see [5, 6] for reviews).

DIC has been used to measure the displacement field in strained specimens and its results were applied to the identification of constitutive laws parameters both for elastic (see e.g. [6]) and hyperelastic materials (e.g. in [7]).

It was also used to study fracture phenomena, mainly in the framework of linear elastic fracture mechanics (LEFM). It was employed to evaluate the stress intensity factors in isotropic [8, 9] and anisotropic [10] materials. LEFM holding, in some neighbourhood of the crack tip the displacements are directly proportional to the stress intensity factors, so there is no need to evaluate the stress or the strain field in order to measure them. On the other hand, to measure the J-integral by employing its definition, it is required to calculate the stress field; in turn this implies making some assumption on the material constitutive model. A DIC measure of the J-integral by domain integration (see e.g. Li et al. [11]) was proposed in [12] for the evaluation of mixed mode stress intensity factors in linear elastic materials. The stresses and the strains had to be evaluated before the J-integral could be calculated. Methods for elasto-plastic materials were recently proposed by Yoneyama et al. [13] both by the evaluation of the stress field and subsequent contour integration and by fitting the displacement field alone to the Hutchinson-Rice-Rosengren solution.

For hyperelastic materials, to the best of the authors’ knowledge, the only attempt at studying fracture via DIC is the work by Mzabi et al. [14], where an ad-hoc criterion for fatigue fracture was proposed, outside of the standard elastic fracture mechanics criteria. For such a class of materials the evaluation of fracture mechanics quantities such as the J -integral may be more complicated than for linear elastic ones. For instance there is no universal solution as the LEFM one, but the solution form and the asymptotic behaviour of the stress or displacement field depend on the constitutive law used. An asymptotic analysis of the elastostatic field near the tip of a crack in a neo-hookean material were given first by Wong and Shield [15]; the case of the so called generalised neo-hookean material was thoroughly dealt with by Geubelle and Knaus [16] and results for a class of Ogden-like materials were obtained by Le and Stumpf [17]. However, as the body of literature on the subject is much more limited than on LEFM, it is not definitely clear how many singular terms there are in the solution and which is the extent of the region they dominate, especially for the more complex models, for which the intricate field equations limit the analysis mostly to the dominant singular term. It is therefore hard to devise strategies relying on the fitting of the displacement field alone to some functional form. It is safer to resort to the J-integral definition and calculate both the stress and the deformation gradient fields. There are many error sources that can interfere in this procedure. Particular concern is caused by those linked to the identification of the material parameters, which must provide a reliable description of the material under all of the stress states, not only under those used to identify the material model parameters. It is known in fact that for material models which are non-linear in the parameters, thus leading to fitting problems which are not necessary convex, a good fit does not automatically grant the ability to reproduce the

actual material behaviour under different conditions (see e.g. [18] for a thorough discussion of these issues).

In this work, the fracture toughness (J-integral) of filled and unfilled natural rubber (NR) compounds was investigated via DIC. A commercial DIC software package (VIC2D by Correlated Solutions, Inc.) was used to measure the displacement field in notched pure shear (PS) specimens and in square specimens under biaxial load. The results were then post-processed using the application programming interfaces provided by the commercial finite element code ABAQUS^{TM} [19], i.e. transforming the results of the DIC analysis into an ABAQUS finite element model, whose nodes correspond to the discrete set of DIC measure points. A similar approach was used by Hild and co-workers [6, 12] with a in-house code.

Ogden's model [20] for incompressible materials was chosen to describe the material behaviour. To identify the material parameters pure shear, uniaxial and equibiaxial tensile tests were run on unnotched specimens. Because of the issues described above, particular care was placed in the validation of the material model by checking its predictive capabilities against experimental data obtained from tests which are independent of the ones used for identification.

The J-integral values obtained by DIC were compared with those from conventional finite element analysis.

After some background information is provided in Section 2, Section 3 gives the details on the experimental part. It will also give details on the finite element simulations of the tests that were run for comparison purposes and on the strategy followed in converting the DIC results into a finite element model (subsection 3.5). Results are eventually presented in section 4.

2. Background

2.1. J-integral evaluation

The J-integral [21] has been widely adopted as a parameter to study the fracture resistance of rubbers (e.g. [22–26]), usually in a purely (non-linear) elastic framework, i.e. in a setting where the only source of dissipation is the creation of new crack surfaces at the crack tip. The fracture criterion in such a framework is a Griffith like one, i.e. fracture is assumed to occur when

$$J = J_c \tag{1}$$

where J_c is the so called toughness or fracture resistance. The fracture process driving force, the J-integral, can be written as contour integral around the crack tip. Assuming a crack propagating in a self similar way, the J-integral is given by

$$J = \int_\gamma \boldsymbol{q}.\boldsymbol{b}.\boldsymbol{n}\, \mathrm{d}\gamma \tag{2}$$

where $\boldsymbol{q}$ is the crack propagation direction unit vector, γ is a contour starting from the lower crack face and ending on the upper one and enclosing the crack tip, $\boldsymbol{n}$ is the vector normal to γ (see Fig.6). γ was defined in the reference configuration, which was used for all the other

calculations as well. In Eq.2 $\boldsymbol{b}$ is the Eshelby's tensor [27, 28], that can be written as

$$\boldsymbol{b} = \boldsymbol{\Psi I} - (\boldsymbol{F} - \boldsymbol{I})^{\boldsymbol{T}}.\boldsymbol{P} \tag{3}$$

where Ψ is the strain energy density, $\boldsymbol{F}$ is the deformation gradient and $\boldsymbol{P}$ the first Piola-Kirchhoff stress tensor. Note that $\boldsymbol{F} - \boldsymbol{I}$ is the displacement field gradient, $\boldsymbol{I}$ being the unit tensor.

In a finite element framework it is rather common to convert the representation in Eq.2 into an area integral by the introduction of a smoothing function [11], so as to use a gaussian integration scheme consistent with the finite element framework, thus relying on the more precise values for the stresses and the strains evaluated at the Gauss' points. Numerical experimentation showed however that in the present case a line integral representation is more than adequate if a sufficient number of points is included in the integration path.

In order for the J -integral to be calculated the strain energy density and the stresses are needed. Thus a constitutive model to describe the stress-strain behaviour of the material must be chosen.

2.2. Ogden's model fitting

It was assumed that the natural rubber compounds used in this study could be described by Ogden's hyperelastic law for incompressibile materials [20], for, among the different models tested (polynomial, Arruda-Boyce, Yeoh), it was the one which gives the best fits to the experimental data and the most stable behaviour (in Drucker's sense).

The corresponding strain energy density is given by

$$\Psi = \sum_{i=1}^{n} \frac{\mu_i}{\gamma_i}\left(\lambda_1^{\gamma_i} + \lambda_2^{\gamma_i} + \lambda_3^{\gamma_i} - 3\right) \tag{4}$$

where λ_j $(j = 1,2,3)$are the principal stretch ratios and μ_i and γ_i, with $i = 1,\ldots,$ n, are material parameters. The number of terms in the sum, n, may be regarded as a material parameter as well, however, it is common practice to fix it *a priori*. Hence there are 2n parameters. In this work n was arbitrarily fixed to 3. The shear modulus in the undeformed configuration, μ, satisfies the following relationship [20]

$$2\mu = \sum_{i=1}^{n} \gamma_i \mu_i \tag{5}$$

According to Reese and Wriggers [29], sufficient conditions for the stability of the material and poly- convexity of the strain energy are (no summation on i):

$$\mu_i \gamma_i > 0 \tag{6a}$$

$$|\gamma i| > 1 \tag{6b}$$

The principal first Piola-Kirchhoff stresses are found from direct differentiation of Eq.4 as [30]:

$$P_i = -\frac{p}{\lambda_i} + \frac{\partial \Psi}{\partial \lambda_i} \tag{7}$$

In the last equation, p is the hydrostatic pressure that can be determined by the stress boundary conditions pertaining to a specific load case [30].

To identify the material parameters the results from the characterisation tests, described in Sec. 3, where fitted simultaneously: following a Least Squares approach the objective function used was defined as

$$f = \sum_{i=1}^{m} \sum_{j=1}^{l} W_{i,j}\left(\bar{P}_{i,j} - P_{i.j}\right) \tag{8}$$

where m is an index representing the test type (pure shear, uniaxial or equibiaxial tensile), $\boldsymbol{j}$ is an index running over all the l experimental data points of the m-th experiment, $\bar{P}_{i,j}$ is the j-th value of the stress measured in the i-th experiment, $P_{i.j}$is the corresponding prediction for a given set of material parameters and $W_{i,j}$are weights corresponding to $1/s^2$, s being the standard deviation of the average stress for a given stretch.

The problem is also subject to the constraints given in Eq.6. In some cases however these constraints were relaxed to check if a better fit could be obtained, and the stability of the identified model verified *a posteriori*.

The Least Squares problem was solved by a custom Python code, basically a wrapper around the non- sorting genetic algorithm NSGAII [31] made available by the Python package pyOpt [32].

It is important to note that since the stresses depend non linearly on the material parameters, there is no guarantee that there is a unique solution to the fitting problem. The identified model may thus be unable to correctly predict the material response when the stress state varies significantly from of the one stress states used during fitting, i.e. the minimum found may not correspond to the actual material behaviour. To check the parameter reliability, an extensive validation is required.

3. Materials and methods

3.1. Materials

Natural rubber (NR0) and two carbon black filled natural rubber compounds (NR25 and NR50) were used in this study. The filled compounds contained 25 and 50 phr of N330 carbon black. The content of sulphur in the rubber was 1.3 phr, and in addition stearic acid (2 phr), tertButyl2benzothiazole (0.8 phr) and Zinc oxide (3 phr) were added to the rubbers for the vulcanisation process. Rubber sheets were compression molded at 160 ◦C and 8 MPa for 15 min so as to assure complete sulfur vulcanization. Uniaxial tensile test pieces were cut using a die from flat sheets, while biaxial and pure shear specimens (see section 3.2) were compression moulded in specially devised moulds. The thickness of the rubber sheets was B=1 mm.

3.2. Characterisation Tests

In order to identify the constants needed for the constitutive modelling, three types of tests were employed.

Uniaxial tensile tests were run using a dumbbell test specimen as prescribed by ASTM D638 (type B-IV). These tests are described in [33], to which the reader is referred for the results.

Pure shear tests were run on unnotched specimens ($a_0 = 0$) with the shape shown in figure 1, using a gauge length h of 10mm. As it can be seen, at the edge of the long sides the cross section thickness was increased with respect to the rest of the specimen. The thicker regions were fitted into a specially devised clamp which avoided slippage, and greatly reduced the flow of material from the gripped zone into the free zone. These tests were run on an Instron 5800 dynamometer at a prescribed crosshead speed of 30 mm min−1 (which provides a strain rate similar to that of the tensile tests). The nominal stress-stretch traces are shown in Fig.8(a) (symbols).

Equibiaxial tensile tests were performed on unnotched ($2a_0 = 0$) square specimens 2(a). The specimen edges are thicker than the rest, in order to connect the specimen to a biaxial dynamometer using the same gripping technique adopted for PS tests. Five separate mounting positions were prepared for each side of the specimen, corresponding to the five clamps on each side of the clamping system, by cutting the thick edge. At the end of each cut a circular hole was cut in the specimen to reduce the stress concentration. Similar solutions have been adopted in the past for biaxial tensile tests [34, 35]. Nevertheless it is to be noted these cuts acts as stress raiser, reducing the range of strains for which the biaxial material behaviour can be measured, as they cause premature failure at the edges.

The tests were run on a custom-built dynamometer; the experimental setup can be seen in Fig. 2(b). The dynamometer axes are all independent thus allowing studying every possible biaxial stress state. In this work however only equibiaxial data will be shown and used. The crosshead displacement rate was 60 mm min^{-1}.

Further details on the biaxial dynamometer can be found in [36]; in the same reference the results of some preliminary tests run on the dynamometer are reported. They show that the stress state is fairly uniform (with the exception of a small region near the border) and that the equibiaxial stress-stretch relationship of the material can be measured just by taking the crosshead displacement to calculate the stretch ratios and the ratio of the load over the nominal cross section (whose length is 131 mm, Fig.2(a)). In fact, using such definitions the results obtained on the biaxial dynamometer for uniaxial tensile and pure shear stress states agreed with those obtained on the standard specimens [36]. Typical stress-stretch response under equi-biaxial conditions is shown in Fig.8(b) (symbols).

3.3. Fracture Tests

Two mode I configurations were used.

The first is a pure shear one, Fig.1, with an edge notch on the mid-plane. For fracture tests, h was set to 13 mm. The edge notch was made by using a sharp razor blade and its length, a_0, was chosen to be 16 mm; as this is longer than the height of the specimen, such a length should give a crack driving force which is almost independent of the crack length, according to Yeoh [37], i.e. should be enough to neglect edge effects by approaching the case of a slab extending to infinity along x. The negligible influence of the free edges on the strain field was also checked by DIC [36].

For the pure shear specimen the J-integral can be easily evaluated as [38, 39]:

$$J = \frac{U}{B(W-a)} \tag{9}$$

where a is the crack length, W the specimen width and U is the work done by the external forces.

Each test was video-recorded with a 10 Megapixels CCD, at a frame rate of 3 fps and a resolution of 82.5 pixels/mm. During the test the camera could not move with respect to the dynamometer crosshead, thus it was not able to follow the specimen during deformation. Therefore a large field of view had to be used in order to be able to keep the specimen inside it from the beginning of the test up to fracture. However this set-up negatively affected the precision of the displacements measured by DIC in the initial stages of the test, when the overall displacements were small.

In order to measure the displacement field via DIC a random speckle pattern was drawn on the specimens with a water based metal grey paint, sprinkled by an airbrush. For the correlation analysis the step size between subsets was chosen to be 6×10^{-2} mm, subset size being about 0.4 mm

Three replicates per test were made.

Some notched biaxial fracture specimens were also used, see Fig.2(a); a 16 mm long notch at the centre (along the x direction) was inserted by a sharp razor blade mounted on a special fixture. In some special cases also notches with initial length $a_0$of 4 and 8 mm were considered.

Although such a setup can be used to test specimens under different biaxility conditions [36], in this work only the results obtained for conditions analogous to the pure shear test will be considered. These are reproduced by imposing zero displacement along the x-axis, while applying a constant displacement rate along the y-direction, up to fracture. In this way the results from the two test geometries could be directly compared; results under different biaxility conditions will be used only for the validation of the constitutive model. The crosshead displacement rate was 1 mm s^{-1}.

For DIC measurements, tests were video recorded with a 10 Mpixel CCD camera at a frame rate of 1 fps and with a resolution of 34 px/mm. The step size was about 0.15 mm, with subset size 0.6 mm. In this case the camera was fixed with respect to the crack, whose position during the test remains centred at the centre of the dynamometer (see Fig.2(b))

There is no known analytic solution giving the J-integral for this specimen, so as a reference value the one calculated via FE simulations was used (see Sec.3.4).

As to the fracture behaviour of the investigated materials, it should be noted that the filled compounds exhibited sideways crack propagation [40], i.e. before initiation and propagation of the main crack along its original direction, small lateral cracks grew. These sideways cracks originated more or less at the original tip, and propagated in a stable way along a curved path which starts almost perpendicular to the initial crack and then tends to rotate backwards. Fig.3 shows the deformed shape assumed by a crack after sideways crack propagation in a NR50 PS sample, just before initiation of the main crack. The sideways crack tips are indicated by the arrows.

In PS tests, for NR25 sideways propagation stopped very early, sideways crack length being shorter than about 0.1 mm, while, for NR50, the sideways crack length before initiation of the main crack could reach about a millimeter.

These cracks have a tremendous impact on the fracture resistance, effectively shielding the original tip from the stresses [41]. For instance, if sideways cracks were assumed to develop exactly at the original crack tip, a wedge-like strain energy singularity would be left there. If the material were linear, rather than the usual $1/r$ strain energy singularity a weaker one would develop, and the same can be conjectured for hyperelastic materials (asymptotic solutions for the wedge problem in neo-hookean materials can be found in [42]; for these materials the conjecture holds). Such a singularity wouldn't be strong enough to lead to a non-vanishing J-integral.

To tackle such a problem, the framework of purely elastic fracture mechanics is too narrow and should be abandoned, for instance by introducing a proper non-linear Dudgale like process zone ahead of the main crack, but this was not attempted in this work and a simpler approach was pursued. Nonetheless, provided the integration path is sufficiently wide to enclose the sideways crack, the J -integral can still be evaluated and interpreted as the resultant of the material forces acting on all the defects present in the domain enclosed by the integration path (compare with [27]). Although such an approach cannot provide a measure of the actual material crack resistance, it can still be used to evaluate the proposed measuring technique and give an apparent toughness value.

3.4. Finite element simulations

To calculate the J -integral for the fracture specimens, FE models were developed using the commercial FE package ABAQUS [19].

Fig.4(a) shows a detail of the mesh used for the PS fracture specimen near the crack tip (overall dimensions are given in Fig.1). The gripped region, i.e. the thicker part, was not modelled and a 2D model was used. Due to symmetry only half of the specimen was modelled. As the thickness of the specimens was

about 1 mm, a plane stress model was used. In a region of radius $1 \times 10{-}1$ mm centred at the crack tip, elements with a characteristic length of about $5 \times 10{-}3$ mm were used. Outside of such a region, concentric rings of elements with side length increasing in a logarithmic fashion were used, up to a radius of 5 mm. A free meshing technique was used elsewhere. Eight-noded rectangular elements were used (CPS8 in ABAQUS). A convergence study was run checking convergence of the predicted load and of the J -integral. The selected mesh comprised about 3600 elements.To simplify the collection of results, a boundary displacement rate in the y-direction (see Fig.1) was applied to the upper boundary of the specimen. The displacements along the x direction at the upper boundary were forced to be zero to reproduce the gripping conditions, however this had little influence on the load-displacement traces predicted by the FE model. Symmetry conditions where applied on the crack plane.

As to the biaxial fracture tests, modelling the boundary conditions depicted in Fig.2(b) would have been very complicated. To keep the model simple, only a rectangular slab with dimensions 60 mm x 22 mm, whose mesh is shown in Fig.4(b), was modelled. The slab is

centred on the crack and near the right crack tip, where the J-integral was evaluated, meshing was the same as for the PS case. A slightly coarser mesh was used for the left crack tip. The elements used were the same as in the PS model. As to the boundary conditions, the very same displacements measured by DIC were applied on the exterior boundary of the FE model by exploiting ABAQUS submodelling technique [19], after conversion of the DIC results to an ABAQUS database (Sec.3.5).

Using this approach, it is not possible to predict the boundary loads and to compare them with the experimental ones. In order to be able to make a comparison of some global quantities to get an estimate of the reliability of the simulations, the major and the minor diameters of the deformed crack were chosen (see Sec.4.1). A mesh convergence study was run by monitoring the convergence of these variables; the study lead to a model containing about 5800 elements.

The simulations were run for a time corresponding to the fracture time, defined as the initiation of propagation of the main in crack in the direction parallel to the initial notch, as determined from the video-recordings.

For both the models, sideways cracks were not modelled.

The evaluation of the J-integral was carried out by using ABAQUS built-in routine, which uses domain integration [19]. The values obtained using the method described in this subsection will be simply referred as “from FEM” in what follows.

3.5. Conversion of DIC data into a finite element framework

In this work the DIC commercial software package VIC2D by Correlated Solutions, Inc. was used to extract the displacement fields of the tested specimens (see Sec.3).

The results obtained from the DIC analysis are a set of displacements at some discrete points in space, on a regular grid whose spacing is basically given by the step size [1]. In order to evaluate the strains and the stresses a set of Python routines was developed to convert DIC measurements to an ABAQUS database, *i.e.* a data structure essentially storing mesh geometry and field values, by using the programming interfaces provided by ABAQUS itself. In this way it was possible to exploit, for differentiation and integration, the robust interpolation scheme provided by the finite element method (as was already suggested by other authors [8]), exploit the powerful ABAQUS visualisation and post-processing capabilities and obtain a very simple mean of driving simulations of sub-regions of the specimen by specifying the displacements measured by DIC (see Sec.3.4).

For each point where the DIC analysis provides a result, a node is generated at the point’s coordinates in the reference configuration (provided by DIC as well); in this work to join them into elements, Delauny’s triangulation was used in order to define first order, plane stress triangular elements (CPS3 in ABAQUS). The triangulation is performed using the facilities provided by the SciPy [43] Python package. Because of intrinsic routine limitations it is not possible to triangulate a concave set, so the routines creates elements which join the crack faces or other spots where correlation gets lost during the analysis. Outside of the crack region this is not a problem since the FE scheme can provide interpolated values for the displacement fields. For the elements bridging the crack faces on the other hand, the deformation gradient is of course artificially very high, but they can be easily excluded from processing using ABAQUS post-processing capabilities. A possible

alternative could be to insert, rather than standard FE, some extended finite elements (X-FE), that can model strong displacement discontinuity [44].

The results of the conversion procedure are illustrated in Fig.5, using a biaxial fracture specimen as an example. Fig.5(a) shows a detail of the crack region in a NR50 specimen; the undeformed configuration is shown. The contour plot gives the vertical displacement v in pixels, at the onset of the main crack propagation. Note that around the crack region, and in particular at the tip, there is a black area for which there are no data. As the crack is a boundary region, correlation cannot be established there, and is immediately lost. Some other spots were correlation is lost can be seen too. Fig.5(b) shows the same region (undeformed configuration) after conversion to an ABAQUS model; the finite element edges are shown superposed to the horizontal displacement (converted to mm). As noted before, there are elements bridging the regions where correlation is lost.

Once the displacement values are defined at the nodes, using the standard FE procedure the displacement field is interpolated over each element with adequate elements shape functions as $\boldsymbol{u} = \boldsymbol{N}.\overline{\boldsymbol{u}}$ where $\boldsymbol{N}$ is the shape functions matrix and $\overline{\boldsymbol{u}}$ are the nodal values; the deformation gradient can be calculated, both at nodes and at Gauss' points as

$$\boldsymbol{F} = \nabla \otimes \boldsymbol{N}.\overline{\boldsymbol{u}} - \boldsymbol{I} \tag{10}$$

where the gradient is to be taken with respect to reference configuration coordinates. From the deformation gradient spectral representation [30] and Eq.4 the evaluation of the stresses and of the Eshelby's tensor follows straightforwardly.

As to the evaluation of the J-integral, in this work attention will be confined to square counter clock-wise paths centred around one of the crack tips (Fig.6), for the sake of simplicity. These paths are completely defined by r, i.e. half the path side length. When needed a normalised curvilinear abscissa along the path will be denoted by s. The correlation loss near the crack faces implies that no displacement data will be available there; it will be shown in the following section that this is of no consequence for an accurate evaluation of the J-integral.

The displacement field resulting from the DIC analysis are, generally speaking, noisy. Although the differentiation operations needed to compute the stresses are conducted using the FE interpolation scheme, the results may turn out to be extremely noisy.

As an example, Fig.7 shows for a NR0 PS fracture specimen some results taken along a path with r = 2 mm, at fracture initiation. Both the magnitude of the displacement vector and the b_{22} component of the Eshelby's tensor (see Fig.6 for the reference system) are shown by dashed lines. While the displacement magnitude seems rather smooth, differentiation and further elaboration of the data lead to a very noisy Eshelby's tensor. It could be therefore thought that it would be better to smooth the displacement data before post-processing. This was attempted in this work using third order bivariate splines; the interpolation was performed using SciPy [43] SmoothBivariateSpline function. As it can be seen looking at the continuous lines in Fig.7, the resulting Eshelby tensor component is actually much smoother. The effect of smoothing on the evaluation of the J-integral is discussed in the next section.

The values obtained using the method described in this subsection will be simply referred as

from DIC in what follows.

4. Results

4.1. Constitutive law identification

The parameters, simultaneously identified from pure shear, uniaxial and equibiaxial tensile tests, are shown in Table 1. In order to get a good fit for NR0 and NR50, some of the constraints in Eq.6 were relaxed. Anyway the given parameters make the model stable for all strains.

Solid lines in Fig.8 show the results of the fitting procedure for the PS and equibiaxial tensile tests. The identified parameters give a fair description of material behaviour for all the three materials examined. Similar results were obtained for the uniaxial tensile tests.

In order to validate the predictive abilities of the identified parameter sets, FE simulations were run on PS fracture specimens as described in section 3.4 and the predicted load-displacement traces checked against the experimental ones.

Selected results for PS notched specimens are shown in Fig.9(a). The agreement is good for all the materials. Note that, for NR25, propagation after the main crack initiation was somewhat stable, while it was unstable for the other materials. Of course the simulations were stopped at the initiation time as detected by the test video-recordings.

For the case of the biaxial fracture specimen, due to the modelling choices made, it is not possible to directly compare the load-displacement traces. To compare predicted and measured quantities, the diameters of the deformed crack configurations where chosen; these were obtained under different biaxility conditions, at fracture initiation [36]. In Fig.9(b) the predicted major (asterisks) and minor diameters (crosses) of the deformed crack shape are plotted against the corresponding measured values, taken at fracture onset or at sideways crack onset if it takes place. The agreement is very good, with errors always below 10%.

Further model validation was made by comparison of the J_c-integral values obtained from the experimental load traces using Eq. 9 with those obtained from FE simulations for PS fracture specimens (Table 2). The results are well matched, taking into account the large scatter in experimental fracture loads.

From the previous results it can be concluded that Ogden's model and the identified material parameters can provide a satisfactory description of the materials under study.

4.2. Evaluation of the J-integral from DIC results

Beginning with pure shear fracture tests, Fig.10 shows the results for the J-integral, evaluated on various contours (half side width r), and at some values of the boundary displacement δ_y , obtained on samples made with NR0, NR25 and NR50 respectively. The filled symbols represent values calculated by using the raw displacements as extracted from the DIC analysis, while the open ones were calculated after the displacement field had been smoothed. Dashed lines are the values from the FE simulations.

As for the case of the J-integral calculation in a FE framework (e.g. [19, 45]), it is expected that for short paths the estimate may be not precise, in the present case, because of

the relatively small number of points along the integration path. Therefore it was expected that the J-integral value becomes truly path independent only for sufficiently large values of r. This is what can actually be seen in Fig.10. However convergence of the J -integral with path size is rather fast: for paths with $r > 2$ mm, which is almost twice the longest sideways crack observed in NR50, the value becomes stationary. For $r = 2$ mm, the integration path contains about 270 points. Note that in the cases of NR0 and NR25, for which there are no sideways cracks or they are very small, the value of the J-integral regularly increases with increasing r up to the converged one. Convergence is not always from below in the case of NR50. This might be related to the fact that shorter paths include part of the sideways cracks, if the boundary displacement is large enough for them to initiate.

Smoothing does not seem to affect the results if a sufficiently long path is taken, nor it influences the convergence rate: the smoothing implied by integration seems to be enough to provide reliable values even starting from the noisy DIC data, which lead to very noisy integrands (see Fig.7). For this reason, raw displacement data will be used henceforth.

The results compare fairly well with those from the finite element simulations, for all the displacement levels shown. To get a quantitative estimate of the agreement, the values of the J-integral from DIC were measured for six boundary displacement values on four contours with $r \geq 2$ and averaged. The values obtained by the two methods are plotted one against the other in Fig.11 (symbols); a log-scale is employed for convenience. In addition the thin grey line gives the bisector of the first quadrant and the black thick line is a linear fit of the data (forced through the origin). The correlation coefficient of the fit is $R^2 = 0.994$ giving a good correlation. Anyway it should be noted that there is a clear difference between the values at low J (and consequently at low values of the applied displacement). This was expected because of the optical set-up used, which could not follow the crack tip during deformation (compare with section 3.3), so that higher errors can be foreseen in DIC displacement fields for low values of δ_y.

At larger values of the applied displacement the difference levels off and is mostly confined into a ±10% band.

Fracture toughness values obtained for pure shear fracture specimens are reported in Table 2 (third column). The estimated mean values are well in line with the results from FE simulation and with those obtained from the infinite slab analytical solution, the differences in the average values being below 10%. The good agreement holds also for NR50, although sideways crack propagation took place in specimens made of this compound. Anyway it should be noted that while the sideways crack length could reach about 0.8 mm, their size is small relatively to the main crack length a_0.

The estimates of the standard deviation of the sample, which are given in parentheses, are similar for all the three methods. They are large, reflecting the large scatter in the initiation load which was experimentally observed.

Similar results were obtained by considering biaxial fracture specimens made with NR0 and NR25. In Fig.12(a) a plot analogous to those in Fig.10 is presented for NR25. The same features obtained with PS fracture tests can be seen: there is no significant difference between the applied J calculated by using smoothed or raw DIC data; convergence is rather fast and almost achieved for $r \geq 2$ mm, and the results compare well with the finite element

reference solution.

As toJ_c, it is the one corresponding in Fig.12(a) to δ_y = 53 mm. Although it is slightly lower than the one obtained with PS fracture specimens (Tab. 2), it is still comparable. For NR0 on the other hand the value obtained from the single specimen tested was 11 N/mm, in line with the results from PS tests taking into account the large dispersion.

Different results were obtained instead for the last compound, NR50. Fig.12(b), where the values of the applied J versus the boundary displacement are reported, shows that for the reference crack length (a_0 = 8 mm) there is a very good agreement between the J values from FEM and from DIC, at low values of boundary displacement and almost up to fracture. However toughness (the last point of the curve) is well below the one obtained with the pure shear test: it is about 50% smaller. To check the independence of the results from the geometry, two tests at varying the initial crack length were run for a_0 4 mm and 2 mm respectively.

J results for the tests with shorter crack length are also shown in Fig.12(b). DIC results shown rather than being averages for different values of r as before, were calculated on the largest possible contour ($r = a_0$). The value at fracture initiation obtained by FE simulations is the same for the three crack lengths; this is an indication that, independently of a_0, fracture is to some extent controlled by J, the applied boundary displacement being such as to give rise to an identical apparent strain energy release rate. However the apparent toughness value determined is not consistent with the one from the PS test, and it was thought that this could be related to presence of sideways cracks, which are not included in the FE models.

The sideways crack length was measured for these samples from DIC. It was noted that with respect to the PS tests, the ratio of the estimated maximum sideways length to the initial crack length was generally larger: while for PS specimens it is about 0.04, for the square specimens it was found to be about 0.1, 0.25 and 0.75 for a_0 equal to 8, 4 and 2 mm respectively.

The fact that J_c appears to be lower than for the PS test is in line with the qualitative idea that the longer the sideways cracks are the more they shield the main crack.

As to the results from DIC, up to some boundary displacement value, they match perfectly the ones obtained via FEM. They become significantly different only some time after the onset of sideways cracks, consistently with the observation on PS specimens that short sideways cracks have no noticeable effect.

For large values of the displacement, DIC results diverge consistently and seem to suggest a larger value for J_c than that estimated by FEM. While it is not clear if such a result can be definitely related to sideways crack presence (some path dependence was noted on the results at larger δ_y), the problems induced by their presence call for some further studies, aimed for instance at clarifying the relationship between the applied J and their length, which are outside of the scope of this work.

5. Conclusions

The number of steps which are needed to calculate toughness values from displacement

fields measured by digital image correlation is quite large: complex non-linear constitutive laws must be identified and validated, by itself a non-trivial task; the measured displacement field must be transformed into a strain field that must be used to calculate a stress field; finally these data can be used to evaluate the J -integral by integration.

Although there are many sources of error that can come into play during this procedure, it has been shown that, in spite of the noise generated by the needed numerical derivatives, DIC data can be used effectively to measure toughness for rubber like materials, within the framework of non-linear elastic fracture mechanics. The viability of the method was shown on two different test configurations.

The convergence of the calculated value of the J-integral with the contour size is relatively fast and the results are well in line with those obtained both by experimental data reduction schemes relying on the (rare) analytic solution available and by FEM techniques.

Both FEM and DIC techniques can be used when there is no analytical solution available, but broadly speaking a DIC analysis requires less effort, as no model of the body geometry is necessary, and it can be applied only to the region containing the crack to be studied.

Acknowledgments

Materials were kindly supplied by Bridgestone Technical Center, Roma, Italy.

References

[1] M. A. Sutton, J.-J. Orteu, H. W. Schreier (2009) Image correlation for shape, motion and deformation measurements, Springer, New York.

[2] P. Burt, C. Yen, X. L. Xu (1982) Local correlation measures for motion analysis: a comparative study., in: Proc. IEEE Conf. on Pattern Recognition and Image Processing p. 269–274.

[3] M. Sutton, W. Wolters, W. Peters, W. Ranson, S. McNeill (1983) Determination of displacements using an improved digital correlation method, Image and Vision Computing 1 (3), 133 – 139. doi: 10.1016/0262-8856(83)90064-1.

[4] T. Chu, W. Ranson, M. Sutton (1985) Applications of digital-image-correlation techniques to experimental mechanics, Experimental Mechanics 25 (3), 232–244. doi:10.1007/BF02325092.

[5] B. Pan, K. Qian, H. Xie, A. Asundi (2009) Two-dimensional digital image correlation for in-plane displacement and strain measurement: a review, Measurement Science and Technology 20 (6).

[6] F. Hild, S. Roux (2006) Digital image correlation: from displacement measurement to identification of elastic properties – a review, Strain 42 (2), 69–80.

[7] L. Chevalier, Y. Marco (2002) Tools for multiaxial validation of behavior laws chosen for modeling hyper-elasticity of rubber-like materials, Polymer Engineering & Science 42 (2), 280–298. doi:10.1002/pen.10948.

[8] S. Roux, F. Hild (2006) Stress intensity factor measurements from digital image correlation: post-processing and integrated approaches, International Journal of Fracture 140 (1-4) 141–157. doi:10.1007/s10704-006-6631-2.

[9] S. Yoneyama, Y. Morimoto, M. Takashi (2006) Automatic evaluation of mixed-mode stress intensity factors utilizing digital image correlation, Strain 42 (1), 21–29. doi:10.1111/j.1475-1305.2006.00246.x.

[10] F. Hou, S. Hong (2014) Characterization of r-curve behavior of translaminar crack growth in cross-ply composite laminates using digital image correlation, Engineering Fracture Mechanics 117, 51–70. doi: 10.1016/j.engfracmech.2014.01.010.

[11] F. Li, C. Shih, A. Needleman (1985) A comparison of methods for calculating energy release rates, Engineering Fracture Mechanics 21 (2), 405–421. doi: 10.1016/0013-7944(85)90029-3.

[12] J. Réthoré, A. Gravouil, F. Morestin, A. Combescure (2005) Estimation of mixed-mode stress intensity factors using digital image correlation and an interaction integral, International Journal of Fracture 132 (1), 65–79. doi:10.1007/ s10704-004-8141-4.

[13] S. Yoneyama, S. Arikawa, S. Kusayanagi, K. Hazumi (2014) Evaluating J-integral from displacement fields measured by digital image correlation, Strain 50 (2), 147–160. doi:10.1111/str.12074.

[14] S. Mzabi, D. Berghezan, S. Roux, F. Hild, C. Creton (2011) A critical local energy release rate criterion for fatigue fracture of elastomers, Journal of Polymer Science Part B: Polymer Phisics 49, 1518–1524. doi:10.1002/polb.22338.

[15] F. S. Wong, R. T. Shield (1969) Large plane deformations of thin elastic sheets of neo-hookean material, Zeitschrift für angewandte Mathematik und Physik 20, 176–199. doi:10.1007/BF01595559.

[16] P. H. Geubelle, W. G. Knauss (1994) Finite strains at the tip of a crack in a sheet of hyperelastic material: I. homogeneous case, Journal of Elasticity 35, 61–98. doi:10.1007/BF00115539.

[17] K. Le, H. Stumpf (1993) The singular elastostatic field due to a crack in rubberlike materials, Journal of Elasticity 32 183–222. doi:10.1007/BF00131660.

[18] R. W. Ogden, G. Saccomandi, I. Sgura (2004) Fitting hyperelastic models to experimental data, Computational Mechanics 34 (6), 484–502.

[19] Simulia Corporation, Abaqus Analysis User's Manual. Version 6.11, Simulia Corp., 2011.

[20] R. W. Ogden (1972) Large deformation isotropic elasticity - on the correlation of theory and experiment for incompressible rubberlike solids, Proceedings of the Royal Society of London. Series A, Mathematical and Physical Sciences 326 (1567), 565–584.

[21] J. R. Rice (1968) A path independent integral and the approximate analysis of strain concentration by notches and cracks, Journal of Applied Mechanics 35 (2), 379–386. doi:10.1115/1.3601206.

[22] K. Tsunoda, J. Busfield, C. Davies, A. Thomas (2000) Effect of materials variables on the tear behaviour of a non-crystallising elastomer, Journal of Materials Science 35 (20), 5187–5198. doi:10.1023/A:1004860522186.

[23] C. Netzker, T. Horst, K. Reincke, R. Behnke, M. Kaliske, G. Heinrich, W. Grellmann (2013) Analysis of stable crack propagation in filled rubber based on a global energy balance, International Journal of Fracture 181 (1), 13–23. doi:10.1007/ s10704-013-9816-5.

[24] A. N. Gent, M. Razzaghi-Kashani, G. R. Hamed (2003) Why do cracks turn sideways?, Rubber Chemistry and Technology 76 (1), 122–131. doi:10.5254/1.3547727.

[25] M. Boggio, C. Marano, M. Rink (2011) Time dependence of fracture behaviour of carbon black filled natural rubber, in: S. Jerrams, N. Murphy (Eds.), Constitutive Models for Rubber VII, CRC Press, London, 363–368.

[26] F. Caimmi, R. Calabrò, C. Marano, M. Rink (2011) Biaxial fracture testing of rubber compounds, in: S. Jerrams, N. Murphy (Eds.), Constitutive Models for Rubber VII, CRC Press, London, 449–454.

[27] J. D. Eshelby (1951) The force on an elastic singularity, Philosophical Transactions of the Royal Society of London. Series A, Mathematical and Physical Sciences 244 (877), 87–112.

[28] P. Chadwick (1975) Applications of an energy-momentum tensor in non-linear elastostatics, Journal of Elasticity 5 (3-4), 249–258. doi:10.1007/BF00126989.

[29] S. Reese, P. Wriggers (1997) Material instabilities of an incompressible elastic cube under triaxial tension, International Journal of Solids and Structures 34 (26), 3433 – 3454. doi:10.1016/S0020-7683(96)00205-3.

[30] G. Holzapfel (2000) Nonlinear Solid Mechanics, Wiley, Chichester, UK.

[31] K. Deb, A. Pratap, S. Agarwal, T. Meyarivan (2002) A fast and elitist

multiobjective genetic algorithm: Nsga-II, Evolutionary Computation, IEEE Transactions on 6 (2), 182–197. doi:10.1109/4235.996017.

[32] R. Perez, P. Jansen, J. Martins (2012) pyopt: a python-based object-oriented framework for nonlinear constrained optimization, Structural and Multidisciplinary Optimization 45 101–118. doi:10.1007/s00158-011-0666-3.

[33] C. Marano, M. Boggio, E. Cazzoni, M. Rink (2014) Fracture phenomenology and toughness of filled natural rubber compounds via the pure shear test specimen, Rubber Chemistry and Technology 87 (3) 501–515. doi:10.5254/rct.14.86950.

[34] C. W. Extrand, A. N. Gent (1991) Strength under various modes of deformation, International Journal of Fracture 48, 281–297.

[35] K. Miller (2000) Testing elastomers for hyperelastic material models in finite element analysis, Tech. rep., Axel Products, Inc.

[36] R. Calabró (2013) Mechanical characterization of elastomers under quasi-static and dynamic biaxial loading conditions, Ph.D. Thesis, Politecnico di Milano, Milano, Italy.

[37] O. Yeoh (2001) Analysis of deformation and fracture of 'pure shear' rubber testpiece, Plastics, rubber and composites 30 (8), 389–397.

[38] N. Hocine, M. Abdelaziz, A. Imad (2002) Fracture problems of rubbers: J-integral estimation based upon η factors and an investigation on the strain energy density distribution as a local criterion, International Journal of Fracture 117 (1), 1–23. doi:10.1023/A:1020967429222.

[39] B. Kim, C. Joe (1989) Single specimen test method for determining fracture energy (jc) of highly deformable materials, Engineering Fracture Mechanics 32 (1), 155–161. doi:10.1016/0013-7944(89)90213-0.

[40] C. Marano, R. Calabrò, M. Rink (2010) Effect of molecular orientation on the fracture behavior of carbon black-filled natural rubber compounds, Journal of Polymer Science Part B: Polymer Physics 48 (13), 1509–1515.

[41] G. R. Hamed (1994) Molecular aspects of the fatigue and fracture of rubber, Rubber Chemistry and Technology 67 (3), 529–536. doi:10.5254/1.3538689.

[42] M. Arfaoui, K. Mansouri, A. Rezgui (2008) An asymptotic finite plane deformation analysis of the elastostatic fields at a notch vertex of an incompressible hyperelastic material, Comptes Rendus Mécanique 336 (9), 737–743. doi:10.1016/j.crme.2008.07.003.

[43] E. Jones, T. Oliphant, P. Peterson, et al. (2001–) SciPy: Open source scientific tools for Python. URL http://www.scipy.org/

[44] S. Roux, J. Réthoré, F. Hild (2009) Digital image correlation and fracture: an advanced technique for estimating stress intensity factors of 2d and 3d cracks, Journal of Physics D: Applied Physics 42 (21), 214004.

[45] P. Gu, M. Dao, R. Asaro (1999) A simplified method for calculating the crack-tip field of functionally graded materials using the domain integral, Journal of applied mechanics 66 (1), 101–108.

Figure Captions

Figure 1: Pure shear test piece used in this work. The thick edges allow clamping without excessive slippage. Nominal dimensions in mm.

Figure 2: Biaxial tensile test (a) Square specimen used for biaxial tests: nominal dimensions in mm. (b) A picture of the biaxial dynamometer with the loading rig used to test square specimens.

Figure 3: NR50 PS fracture sample. Detail of the main crack tip region just before initiation of the main crack, showing sideways cracks (indicated by the arrows)

Figure 4: FE models of fracture specimens. Dimensions in mm. (a) PS fracture specimen: detail of the crack tip region. Only the upper half of the specimen is modelled. (b) biaxial fracture specimens: submodel.

Figure 5: NR50, biaxial fracture specimen. Detail of the crack region with contour plot of the displacement fields at fracture initiation. Both the pictures are referred to the undeformed configuration. (a) Raw data from DIC analysis. (b) Result of the conversion of VIC data to a FEM model.

Figure 6: Scheme of the crack tip in the finite element model resulting from the conversion of DIC data into a FE model. The thick line represents the square paths used for J-integral evaluation

Figure 7: Norm of the displacement field and one of the components of the Eshelby's tensor along a path with r = 2 mm. NR0, PS fracture specimens at initiation time.

Figure 8: Nominal stress vs. stretch ratio curves for the three materials tested (open symbols). Continuous lines are the Ogden's model fits to the experimental data. (a) Pure shear test. (b) Equibiaxial test.

Figure 9: Comparison of the FEM results with the experimental ones for various fracture specimens. (a) Load-displacement traces for notched PS specimens. Symbols: experimental data. Solid lines: FEM predictions. (b) Comparison between the predicted and measured diameters of the deformed cracks for biaxial fracture tests.

Figure 10: Pure shear fracture tests: J-integral values for some values of the boundary displacement. Solid symbols: eval- uated from the raw DIC displacements. Empty symbols: evaluated after DIC displacement smoothing. Dashed lines: FEM predictions. (a) NR0. (b) NR25. (c) NR50.

Figure 11: PS: comparison between FEM and DIC results.

Figure 12: Biaxial fracture tests: J-integral results. (a) NR25, J-integral values for some values of the boundary displacements. Solid symbols: evaluated from the raw DIC displacements. Empty symbols: evaluated after displacement smoothing. Dashed lines: FEM predictions. δ_y = 53 mm corresponds to fracture initiation. (b) NR50, J-integral results for different initial crack lengths.

Tables

Compound	μ_1[MPa]	μ_2 [MPa]	μ_3 [MPa]	γ_1	γ_2	γ_3
NR0	0.39	0.036	-0.038	1.96	5.80	5.77
NR25	0.94	0.041	-3.5e-5	1.00	4.31	-5.65
NR50	1.39	0.29	-1.4e-4	0.78	3.84	-6.96

Table 1: Ogden's model parameters identified for the three compounds.

	Jc [N/mm]		
Compound	analytic	FEM	DIC
NR0	8 (±28%)	9 (±28%)	8 (±23%)
NR25	6 (±19%)	5.4 (±17%)	5 (±21%)
NR50	42 (±12%)	44 (±14%)	41 (±15%)

Table 2: PS fracture test. Apparent toughness values obtained by Eq. 9 (analytic), via FEM and via digital image correlation post-processing, with rough estimates of the standard deviation (three samples).

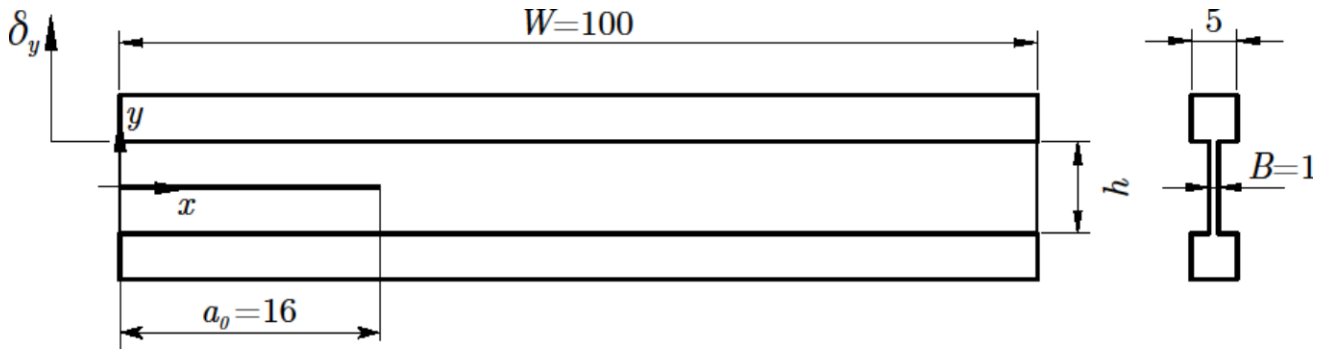

Figure 1

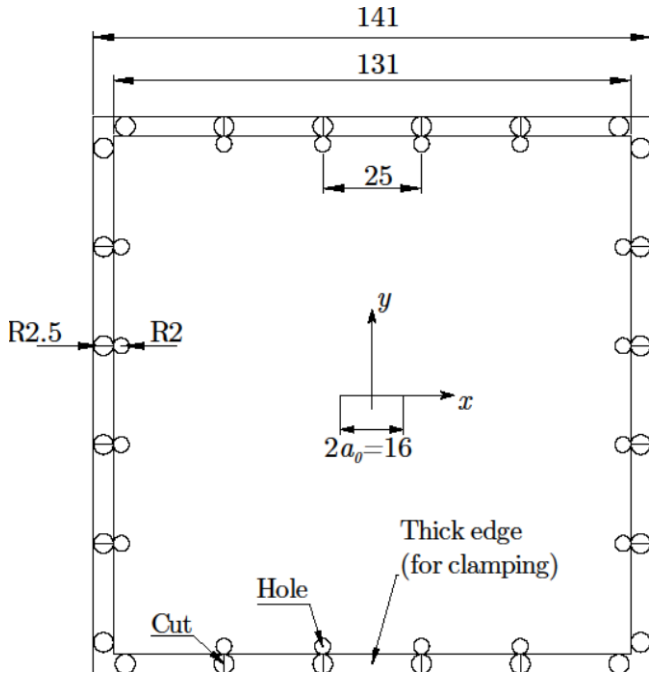

Figure 2a

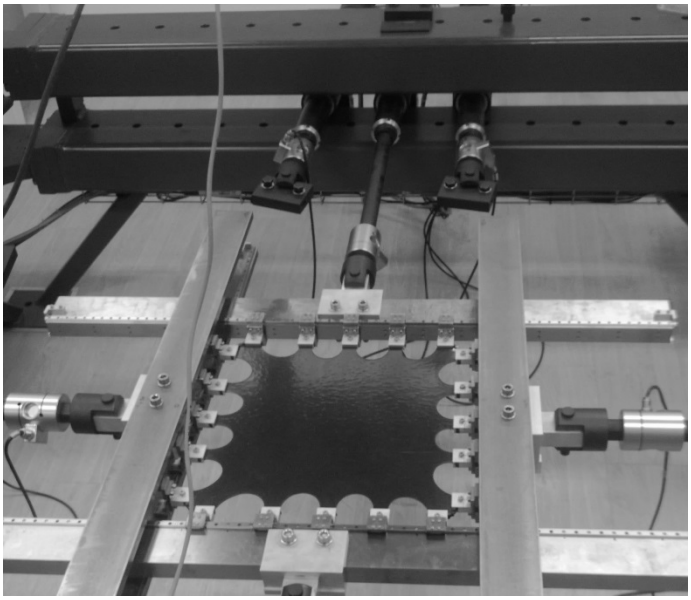

Figure 2b

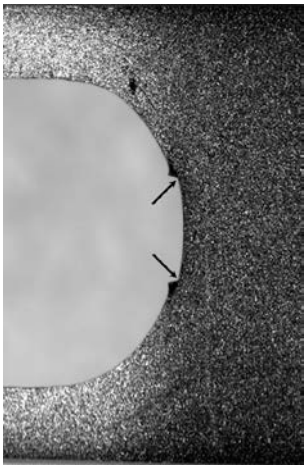

Figure 3

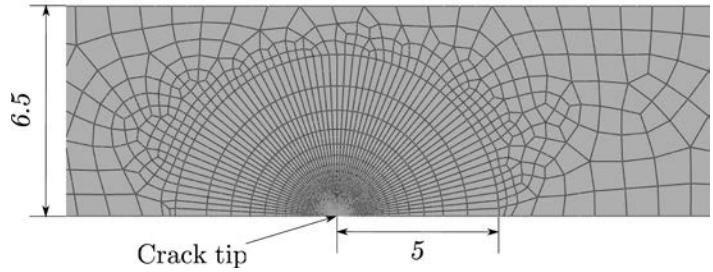

Figure 4a

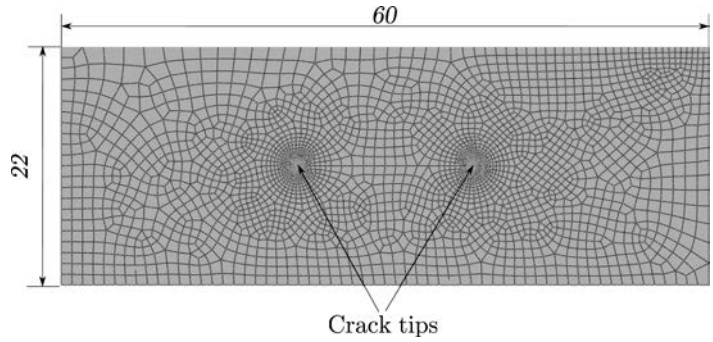

Figure 4b

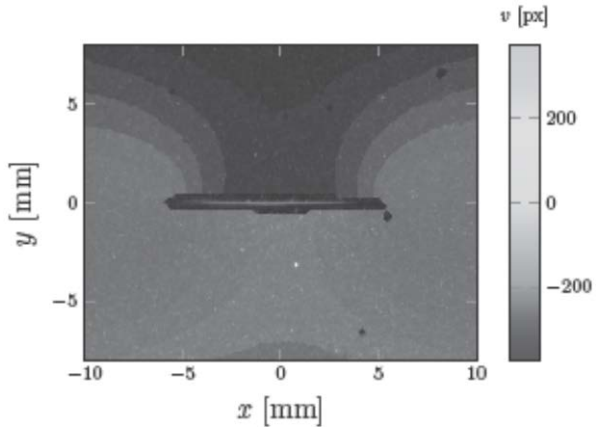

Figure 5a

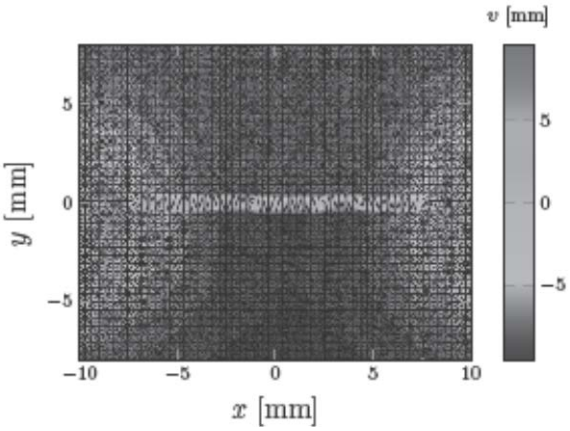

Figure 5b

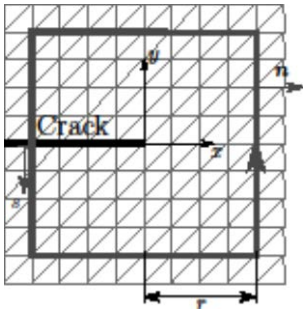

Figure 6

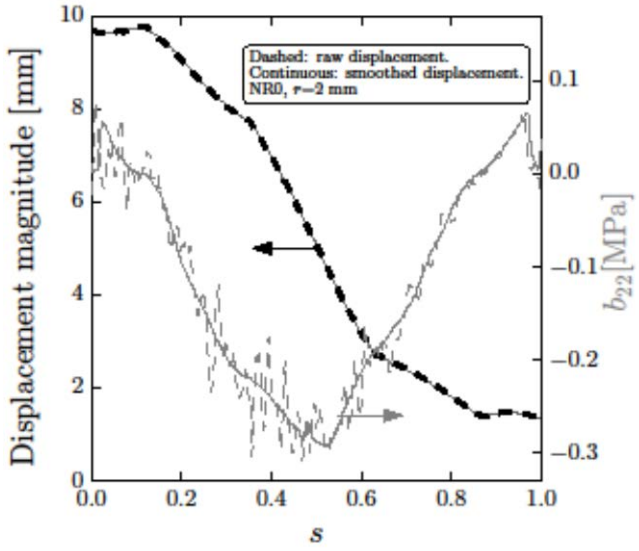

Figure 7

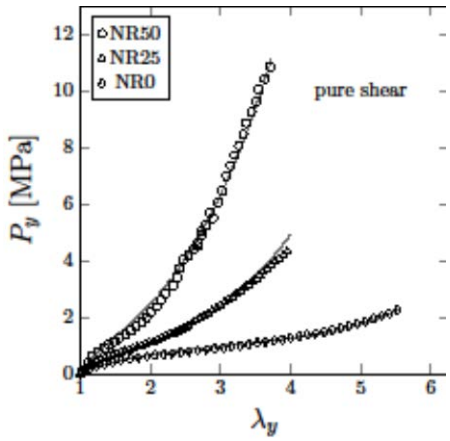

Figure 8a

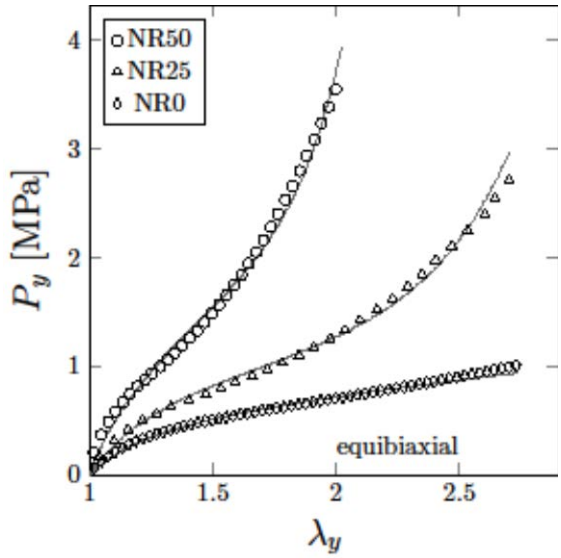

Figure 8b

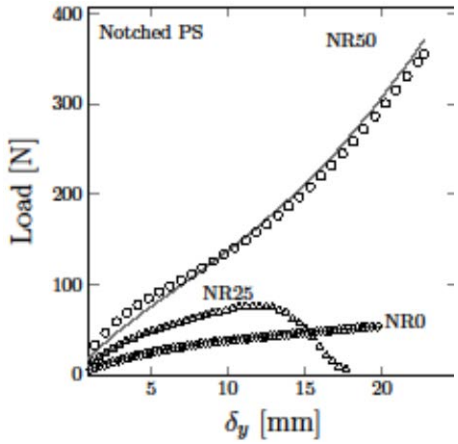

Figure 9a

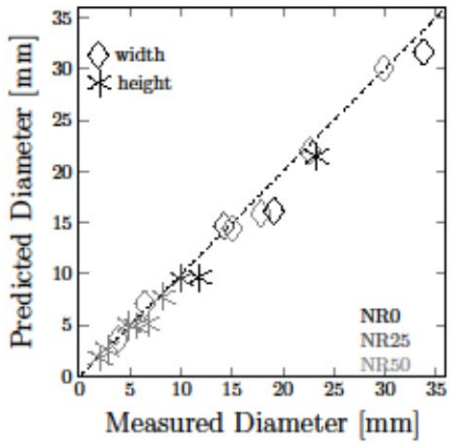

Figure 9b

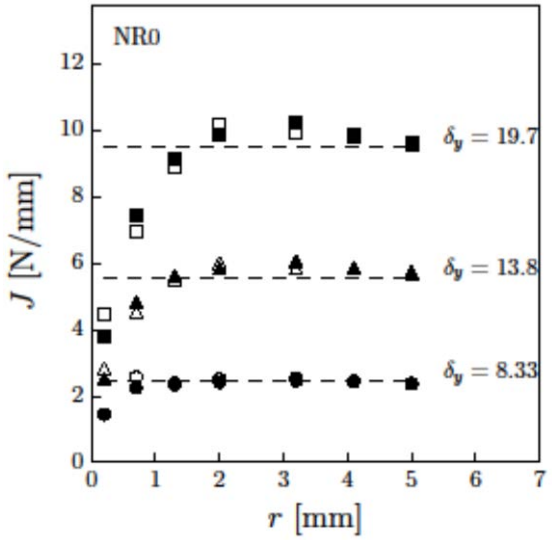

Figure 10a

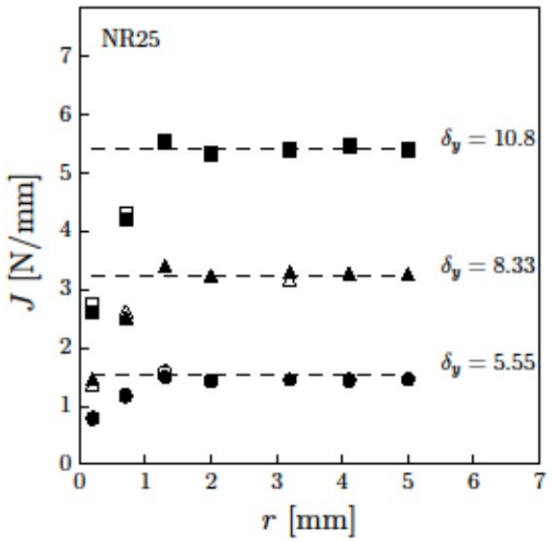

Figure 10b

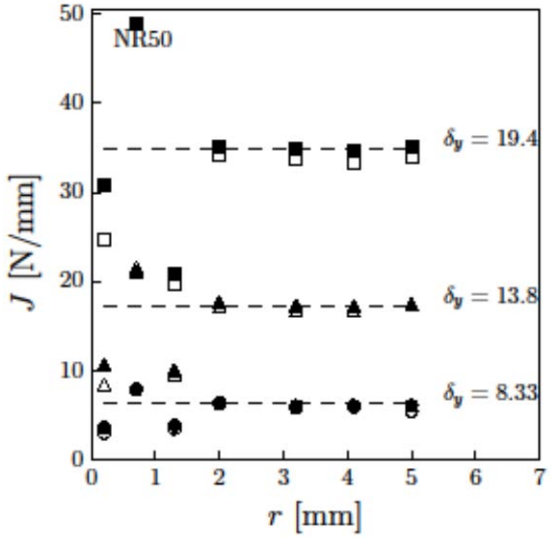

Figure 10c

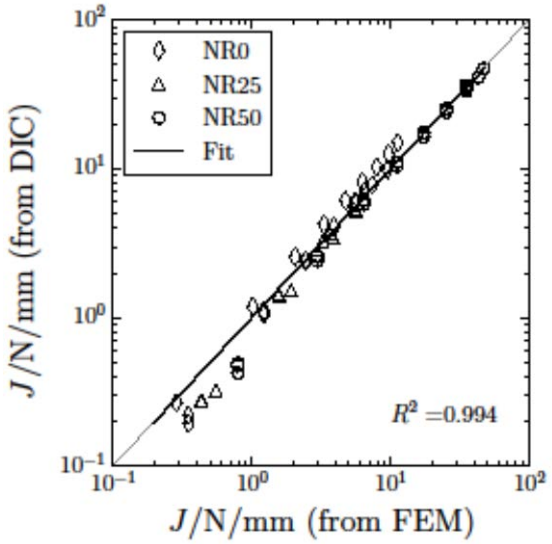

Figure 11

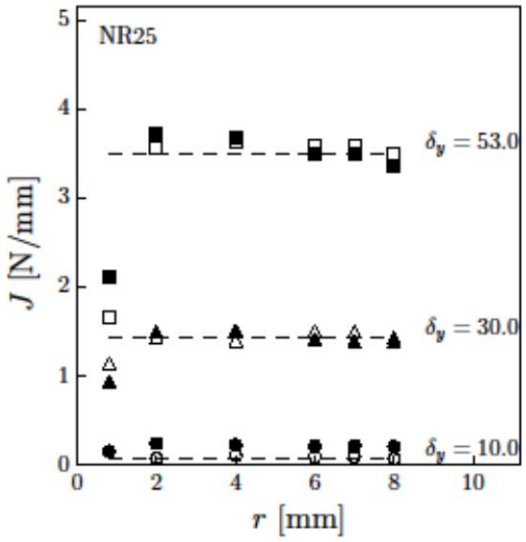

Figure 12a

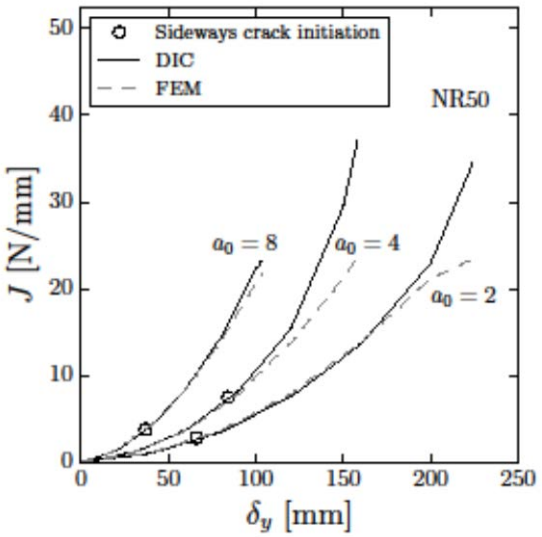

Figure 12b